PHOTONICS Research

Topologically protected long-range coherent energy transfer

Yujing Wang,[1] Jun Ren,[2] Weixuan Zhang,[1] Lu He,[1] ⓘ and Xiangdong Zhang[1,*]

[1]*Key Laboratory of Advanced Optoelectronic Quantum Architecture and Measurements of Ministry of Education, School of Physics, Beijing Institute of Technology, Beijing 100081, China*
[2]*College of Physics and Hebei Key Laboratory of Photophysics Research and Application, Hebei Normal University, Shijiazhuang 050024, China*
Corresponding author: zhangxd@bit.edu.cn

The realization of robust coherent energy transfer with a long range from a donor to an acceptor has many important applications in the field of quantum optics. However, it is hard to be realized using conventional schemes. Here, we demonstrate theoretically that robust energy transfer can be achieved using a photonic crystal platform, which includes the topologically protected edge state and zero-dimensional topological corner cavities. When the donor and the acceptor are put into a pair of separated topological cavities, the energy transfer between them can be fulfilled with the assistance of the topologically protected interface state. Such an energy transfer is robust against various kinds of defects, and can also occur over very long distances, which is very beneficial for biological detections, sensors, quantum information science, and so on.   © 2020 Chinese Laser Press

1. INTRODUCTION

Energy transfer plays an essential role in many processes in nature, such as photosynthesis in the light-harvesting complex of green plants [1,2]. Except for interpreting the energy transfer in nature, manipulating the energy transfer in artificial structures also has many potential applications. For example, white-light emitting nanofiber has been fabricated through efficient energy transfer [3], sensitive and efficient biosensing has been realized by designing novel nanostructures [4], and efficient solar energy conversion can also be achieved by plasmonic nanostructures [5].

In recent years, it has been reported that coherence may play a key role in energy transfer [6–14], and quantum coherence could enhance the efficiency of energy transfer [15–23]. However, under natural circumstances, coherence decreases quickly with the increase in distance; thus, energy transfer efficiency decreases sharply as the distance between two molecules increases, which greatly limits its application in various aspects. How to realize long-range energy transfer with high efficiency is a challenge for us. In addition, even if the long-range energy transfer with high efficiency can be realized, how to keep it stable and free from environmental perturbations is also a problem.

New developments in the field of topological photonics [24–27] make it possible to solve the above-mentioned problems. By introducing topology into the field of optics, numerous fascinating properties, such as the unidirectional backscattering-immune propagation of photonic edge modes

[28–37], can be achieved. The combination of quantum mechanics and topology can bring more intriguing phenomena [38–48], including topological sources of quantum light [39–41], quantum interference of topological states of light [43], topological quantum optics interface [38], topologically robust transport of entangled photons [42], and so on. Recently, a new class of higher-order topological insulators has been theoretically proposed and experimentally demonstrated in many different systems [49–68]. Moreover, the zero-dimensional (0D) topological corner state has been observed in the two-dimensional (2D) photonic crystal (PhC) slab [55,56, 67,68], which provides an ideal platform to design topological nanocavities [67,68].

Motivated by the above investigations, in this work, we provide a scheme to realize long-range energy transfer with high efficiency in the PhC platform. The designed PhC platform possesses a topologically protected edge state and 0D topological corner cavities. When the donor and the acceptor are put into two topological cavities, the energy transfer between them can occur through the topologically protected edge state. Such an energy transfer can always exist, even though the donor and the acceptor are separated by a long distance, and it is robust against disorders.

2. SCHEME AND THEORY

We consider a PhC platform that contains five kinds of integrable modules (I–V) in different regions, as shown in Fig. 1(a).
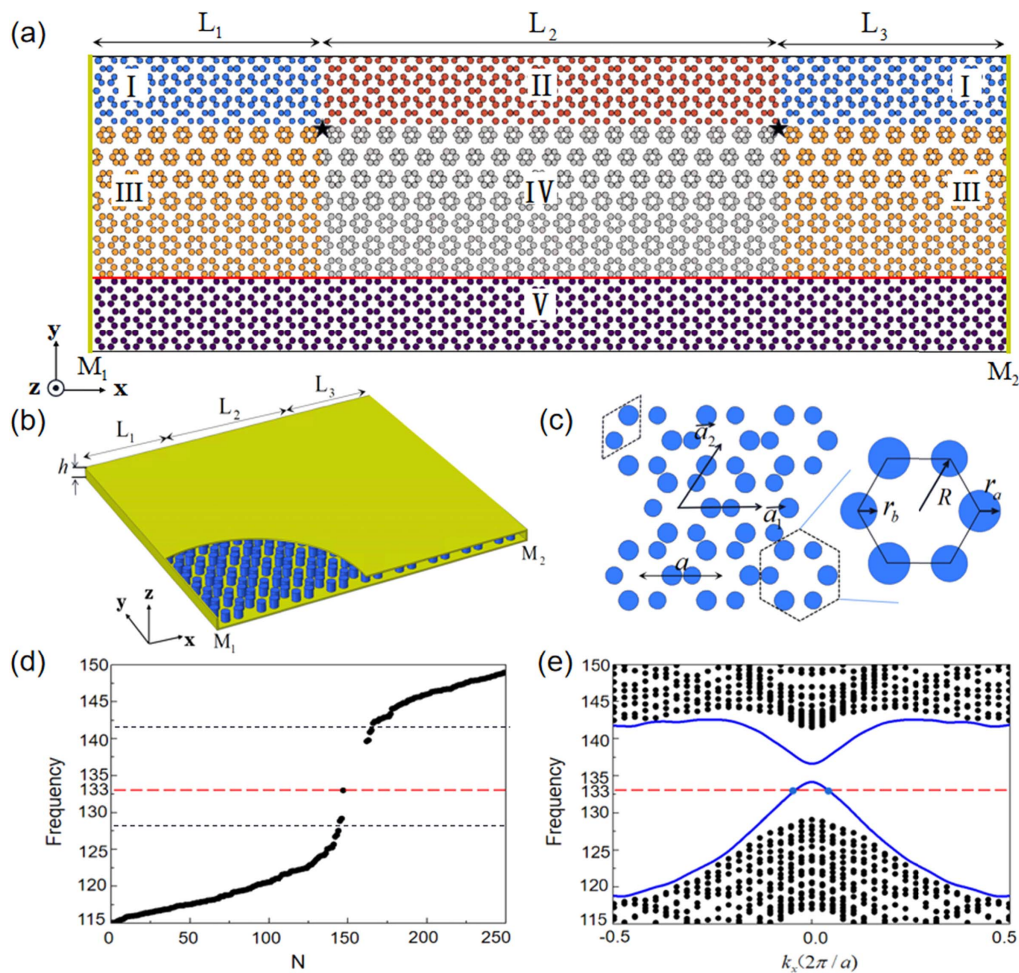
Fig. 1. (a) Simplified top view of the PhC system. The two black pentagrams represent two distant identical topological corner cavities (appearing at the intersections of the I–IV regions), and the red line indicates a topological interface state. (b) Three-dimensional photonic crystals with two pairs of gold plates placed in the xy and yz planes. h is the height of the cylinders. (c) Schematic of a triangular photonic crystal composed of six Al_2O_3 cylinders ($\varepsilon = 7.5$). Right panel: magnified view of the unit cell. The radius of the hexagon (solid black line) is R, while the radius of the large (small) cylinder is marked with r_a (r_b). (d) Eigen-energy spectrum of the topological corner state. (e) Calculated band diagram based on a supercell composed of regions IV and V, where a periodic (absorbing) boundary condition is applied in the x (y) direction. Blue lines are for topological edge states.

Such a platform consists of Al_2O_3 ($\varepsilon = 7.5$) cylinders with various radii embedded in air background. All modules possess a triangular lattice with the lattice constant a being 1.25 µm, and the unit cell contains six Al_2O_3 cylinders. In order to show the system more clearly, the color of cylinders in each region is different. The PhC system is assembled inside a waveguide with two pairs of high-reflectivity metallic plates placed in the xy and yz planes, and the height of these cylinders h is taken as 0.1a, as illustrated in Fig. 1(b).

Figure 1(c) shows the schematic lattice pattern in region I. For convenience, we note that the radius of the larger (smaller) cylinders in the triangular lattice of all regions is marked with r_a (r_b), and the distance from the cylinder center to the center of the unit cell is marked with R. The r_a (r_b) and R in five modules are different. In the region I, the r_a (r_b) is set as 0.14 µm (0.16 µm), and $R = 0.371a$. The lattices in regions I/II and III/IV satisfy the inversion symmetry. In such a case, two topological corner cavities can appear at the crossing of four regions,

as marked by black pentagrams in Fig. 1(a) [66]. Figure 1(d) displays their eigen-energy spectrum, and a state at 133 THz inside the gap of the topological kink states appears.

In order to design the interface state whose frequency matches the resonance frequency of the corner cavity mode, the two high-reflectivity metal plates in the xy plane [marked by M_1 and M_2 in Figs. 1(a) and 1(b)] are set to ensure the density of interface states of the waveguide modified (or discretized) to form Fabry–Perot (FP) waveguide modes. Also, we need to design regions III and IV skillfully, so a gradual change of parameters in different rows of the lattice is applied. Taking region III as an example, the gradually varied radii of the small (large) cylinders r_a (r_b) are 0.14 µm (0.16 µm), 0.1425 µm (0.1575 µm), 0.145 µm (0.155 µm), 0.1475 µm (0.1525 µm), and 0.15 µm (0.15 µm) from the first to fifth rows, and R is set as 0.243a, 0.243a, 0.262a, 0.281a, and 0.3a, respectively. The corner states we designed exist in the coexistence of sublattice symmetry breaking and lattice deformation., while the design

of edge states requires only lattice deformation. If we do not do the gradual change of parameters in regions III and IV, the frequency of the corner state will fall in the gap of the interface state or the bulk state, where the coupling between the corner state and the interface state cannot occur [66]. In addition, the parameters in the sixth and seventh rows are the same as in the fifth row: $r_a = r_b = 0.15$ μm, $R = 0.3a$ ($a/R > 3$). The $r_a = r_b = 0.15$ μm and $R = 0.36a$ ($a/R < 3$) are taken in region V. In such a case, a topologically protected interface state with the working frequency located at 133 THz, which corresponds to the resonance frequency of the corner cavity mode, can be obtained [36,37]. This can be demonstrated by the calculated dispersion relation presented in Fig. 1(e). This gap is a result of the avoided crossing of the interface states caused by their interaction due to the broken C_6 symmetry at the conducting interface. Theoretical and experimental results show that the topological interface mode is still extremely robust, and the backscattering can be ignored [37,69–71]. The distance between two topological corner cavities is L_2, and the distance between the left (right) cavity and the left (right) metallic plates is L_1 (L_3). Here, we consider the transverse magnetic mode with the out-of-plane electric field and the in-plane magnetic field.

We put a pair of two-level molecules into the topological corner cavities. The dynamic process and energy transfer properties between two molecules are studied through a master equation approach. Initially, one of the molecules is excited, and the other in its ground state; they are called donor (D) and acceptor (A), respectively. The corresponding Lindblad master equation of two molecules [19,72–75], whose microscopic origin and derivation using the Born–Markov and rotating-wave approximations can be found in Refs. [73–75], is expressed as follows:

$$\partial_t \rho = \frac{i}{\hbar}[\rho, H] + \frac{\gamma_D + 2\gamma_0}{2}(2\sigma_D \rho \sigma_D^\dagger - \sigma_D^\dagger \sigma_D \rho - \rho \sigma_D^\dagger \sigma_D)$$
$$+ \frac{\gamma_A + 2\kappa}{2}(2\sigma_A \rho \sigma_A^\dagger - \sigma_A^\dagger \sigma_A \rho - \rho \sigma_A^\dagger \sigma_A)$$
$$+ \frac{\gamma_{12}}{2}(2\sigma_D \rho \sigma_A^\dagger - \sigma_D^\dagger \sigma_A \rho - \rho \sigma_D^\dagger \sigma_A)$$
$$+ \frac{\gamma_{21}}{2}(2\sigma_A \rho \sigma_D^\dagger - \sigma_A^\dagger \sigma_D \rho - \rho \sigma_A^\dagger \sigma_D), \quad \text{(1)}$$

where ρ is the density matrix of two molecules, and $\sigma_{D(A)}^\dagger$ and $\sigma_{D(A)}$ are, respectively, the creation and annihilation operators for the donor (acceptor). γ_0 is the natural dissipation in the donor, and κ is the separation rate in the acceptor, and in this work, we have taken $\gamma_0 = 1$ ns^{-1} and $\kappa = 1$ ps^{-1} in our calculations [19]. Due to the symmetry of two cavities, we assume the decay rates of two molecules are the same, namely, $\gamma_D = \gamma_A = \gamma_1$. The γ_{12} represents the incoherent coupling term (interference term) between the two molecules, and we also have $\gamma_{12} = \gamma_{21}$. The γ_D and γ_{12} can be calculated as

$$\gamma_D = \frac{2\omega_0^2}{\varepsilon_0 c^2 \hbar} \text{Im}[\vec{\mu}_D^* \cdot \overset{\leftrightarrow}{G}(\vec{r}_D, \vec{r}_D, \omega) \cdot \vec{\mu}_D], \quad \text{(2)}$$

and

$$\gamma_{12} = \frac{2\omega_0^2}{\varepsilon_0 c^2 \hbar} \text{Im}[\vec{\mu}_A^* \cdot \overset{\leftrightarrow}{G}(\vec{r}_A, \vec{r}_D, \omega) \cdot \vec{\mu}_D]. \quad \text{(3)}$$

In Eqs. (2) and (3), $\overset{\leftrightarrow}{G}(\vec{r}_A, \vec{r}_D, \omega)$ is the classical Green tensor of the system, which is the solution to the tensor equation $[\nabla \times \nabla \times -k_0^2 \varepsilon(\vec{r}, \omega)]\overset{\leftrightarrow}{G}(\vec{r}, \vec{r}'; \omega) = \overset{\leftrightarrow}{I}\delta(\vec{r} - \vec{r}')$, and $\vec{r}_D$ and $\vec{r}_A$ are position vectors of the donor and acceptor, respectively. $\vec{\mu}_D$ and $\vec{\mu}_A$ are dipole moments of two molecules, and in this work, we have taken $|\vec{\mu}_D| = |\vec{\mu}_A| = 6.4 \times 10^{-23}$ C · m. The Hamiltonian of two molecules shown in Eq. (1) can be expressed as

$$H = \sum_{i=D,A} \hbar(\omega_0 + \delta_i)\sigma_i^\dagger \sigma_i + g_{12}(\sigma_D^\dagger \sigma_A + \sigma_A^\dagger \sigma_D), \quad \text{(4)}$$

where g_{12} is the coherent coupling between two molecules, which can be calculated with

$$g_{12} = \frac{\omega_0^2}{\varepsilon_0 \hbar c^2} \text{Re}[\vec{\mu}_A^* \cdot \overset{\leftrightarrow}{G}^s(\vec{r}_A, \vec{r}_D, \omega) \cdot \vec{\mu}_D]. \quad \text{(5)}$$

The Green tensor $\overset{\leftrightarrow}{G}^s(\vec{r}_A, \vec{r}_D, \omega)$ shown in Eq. (5) is the scattering Green tensor of the field dipole located at $\vec{r}_A$ and the source dipole located at $\vec{r}_D$, which can be obtained with

$$\vec{n}_A \cdot \overset{\leftrightarrow}{G}^s(\vec{r}_A, \vec{r}_D, \omega) \cdot \vec{n}_D = -\vec{n}_A \cdot \vec{E}_s(\vec{r}_A)|_{\vec{r}_D}, \quad \text{(6)}$$

where $\vec{n}_A$ and $\vec{n}_D$ represent the direction of the field dipole and source dipole moment, respectively, and $\vec{E}_s(\vec{r}_A)|_{\vec{r}_D}$ represents the scattering electric field at the location of field dipole $\vec{r}_A$ induced by the source dipole located at $\vec{r}_D$.

In this work, the orientation of the source dipole moment is taken as the positive direction of the z axis, which will excite the TM modes of the designed structure, and the electric direction of the field dipole is also parallel to the z axis. In this case, the above equation turns into

$$G_{zz}^s(\vec{r}_A, \vec{r}_D, \omega) = -\vec{E}_z^s(\vec{r}_A)|_{\vec{r}_D}. \quad \text{(7)}$$

Note that an important Markov approximation has been employed in the derivation of Eq. (1), which requires that the coherent couplings between a single molecule and electromagnetic modes are much weaker than the couplings between molecules through the electromagnetic field. In the present work, the main conclusion is obtained when the coherent coupling between the two molecules is much larger than the coupling between the single molecule and electromagnetic field, which satisfies the Markov approximation. Thus, Eq. (1) is valid in this context. Based on Eq. (1) and the calculated parameters shown in Eqs. (2), (3), and (5), we can derive the dynamics of two molecules and investigate the coherent energy transfer between them. There are two important parameters to measure the properties of coherent energy transfer: energy transfer efficiency η and transfer time t_f [19,23,76]:

$$\eta = 2\int_0^\infty \kappa P_A(t)dt, \quad \text{(8)}$$

and

$$t_f = \int_0^\infty t P_A(t)dt \bigg/ \int_0^\infty P_A(t)dt. \quad \text{(9)}$$

The energy transfer efficiency η represents the total probability of excitation used for charge separation, and the energy transfer time means the average waiting time before charge separation happens in the acceptor [19,23,76]. In Eqs. (8) and (9), $P_A(t)$
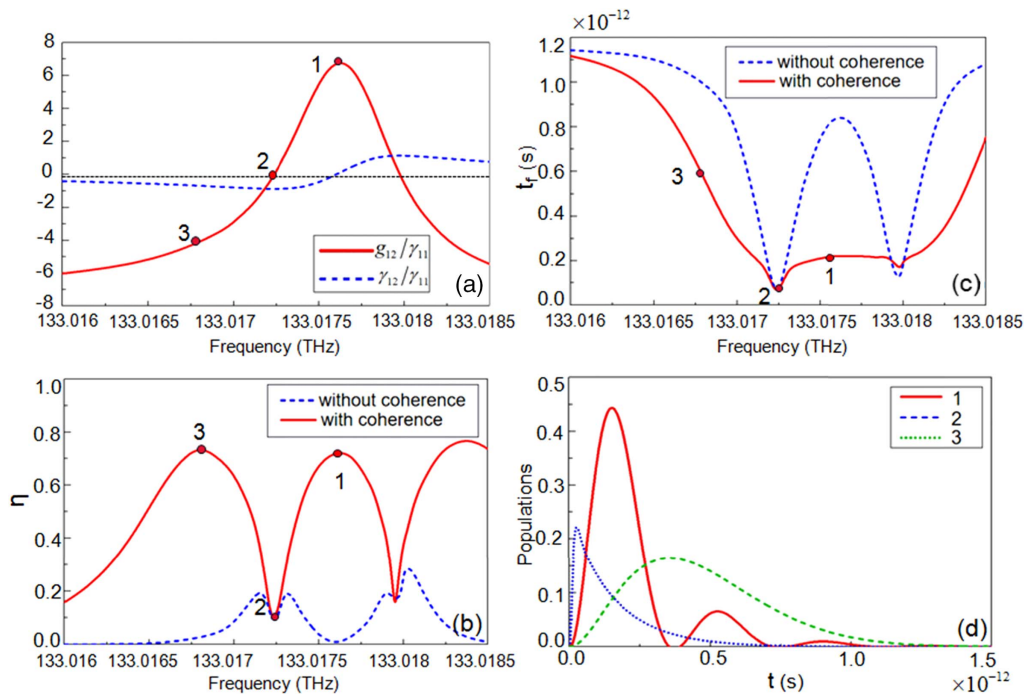
Fig. 2. (a) Coherent (red solid curve) and incoherent (blue dashed curve) couplings between two molecules with parameters $L_2 = 20a$ and $L_1 = L_3 = 19a$. (b) Energy transfer efficiency η and (c) energy transfer time t_f as a function of the frequency with (red solid lines) and without (blue dashed lines) coherent coupling. (d) Populations of acceptor under three typical frequencies marked in (a), (b), and (c).

is the population of the acceptor and represents the probability density of the donor in the ground state, and the acceptor is in the excited state at time t, which is equal to the matrix element $\rho_{22}(t)$ obtained from Eq. (1) under the normal basis ({$|00\rangle$, $|01\rangle$, $|10\rangle$, $|11\rangle$}). Based on Eqs. (8) and (9), we can calculate the coherent energy transfer efficiency and time in the designed system. Note that Eqs. (8) and (9) are derived from Eq. (1), and it can be seen that both of them depend not only on the parameters of the acceptor but also on the parameters of the donor.

3. RESULTS AND DISCUSSION

In this section, we present the calculated results for the coherent energy transfer efficiency and time in our designed PhC platform. One of the advantages of this platform is that the coherent strong coupling is easy to be realized. The red solid line in Fig. 2(a) displays the calculated results of the normalized coherent coupling coefficient (g_{12}/γ_{11}) as a function of the transition frequency. The corresponding incoherent coupling coefficient (γ_{12}/γ_{11}) is shown by blue dashed lines. It is seen clearly that very strong coherent coupling ($g_{12}/\gamma_{11} = 7.005$) can be reached around the frequency $f = 133.0175$ THz; at the same time, the incoherent coupling is almost equal to zero. Under the strong coherent coupling regime, if one of the molecules is excited, the excitation will be transferred back and forth between the two molecules, namely, coherent energy transfer. The energy transfer efficiency η and time t_f are calculated as a function of the frequency for the case of $L_2 = 20a$, and the results are presented in Figs. 2(b) and 2(c), respectively. It is found that when coherent coupling is maximum, energy

transfer efficiency can reach 0.75 [corresponding to the mark "1" in Figs. 2(a)–2(c)], which is much larger than those in other systems [15–23]. At the same time, the energy transfer time is about 200 fs, namely, fast and high-efficiency coherent energy
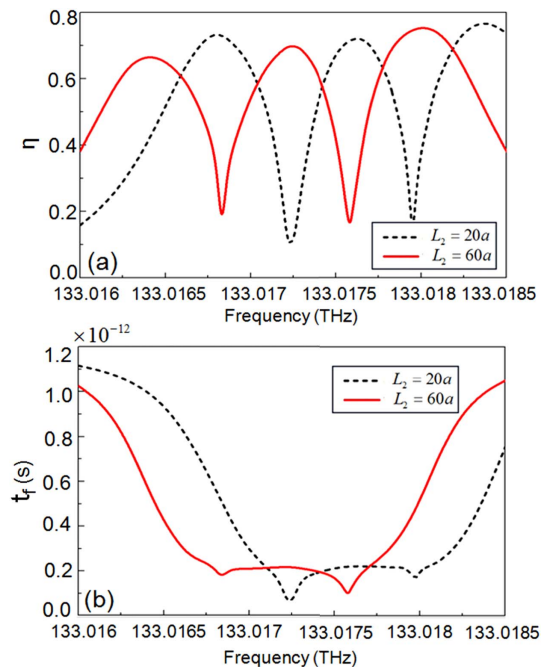
Fig. 3. (a) Energy transfer efficiency and (b) transfer time between two molecules separated by a longer distance $L_2 = 60a$ (red solid lines). The black dashed lines represent the case of $L_2 = 20a$.

transfer is demonstrated in the present PhC platform. In fact, for energy transfer, high transfer efficiency and short transfer time have always been our goal, which is beneficial to sensors, quantum information science, and so on.

We notice that there are two other peaks in energy transfer efficiency, where both the coherent and incoherent couplings are not zero; however, at these two frequencies, the energy transfer times are much longer than at the coherent coupling peak. The reason can be found in Fig. 2(d), where the populations of the acceptor are plotted at three typical frequencies, marked in Figs. 2(a)–2(c). In the case of maximal coherent coupling (marked by "1"), the population of the acceptor (red solid curve) reaches a relatively large value at the beginning. This is because the coherent coupling is proportional to the height of the quantum beat and the beat frequency, while incoherent coupling controls the duration of a single quantum beat. Therefore, the maximal coherent coupling and minimal incoherent coupling not only guarantee larger energy transfer efficiency, but also ensure less energy transfer time. For another efficiency peak (marked by "3"), although the integral of population over time is also large, it is clear that the energy transfer has also undergone a much longer time. The blue dashed curve

represents the case in which the incoherent coupling is maximum and coherent coupling is zero (marked by "2"). Obviously, small coherent coupling leads to a very low quantum beat, which results in a small energy transfer efficiency.

In order to explore the role of coherent coupling played in energy transfer, we plot the results without coherence ($g_{12} = 0$) by blue dashed curves in Figs. 2(b) and 2(c). It is clearly shown that the energy transfer efficiency with coherent coupling is always larger than that without coherent coupling, and the energy transfer time is always shorter than that without coherent coupling. That is to say, coherent coupling always helps increase energy transfer efficiency while reducing energy transfer time.

The important feature of this platform is that the realized energy transfer can maintain a very long distance. The red lines in Figs. 3(a) and 3(b) represent the calculated results of coherent energy transfer efficiency and time for the case with $L_2 = 60a$. For comparison, the corresponding results for the case with $L_2 = 20a$ are shown by black dashed lines. Obviously, the increase in distance allows only a slight decrease in efficiency and a slight increase in transfer time, except for the frequency shift presented. The frequency shift is due to the
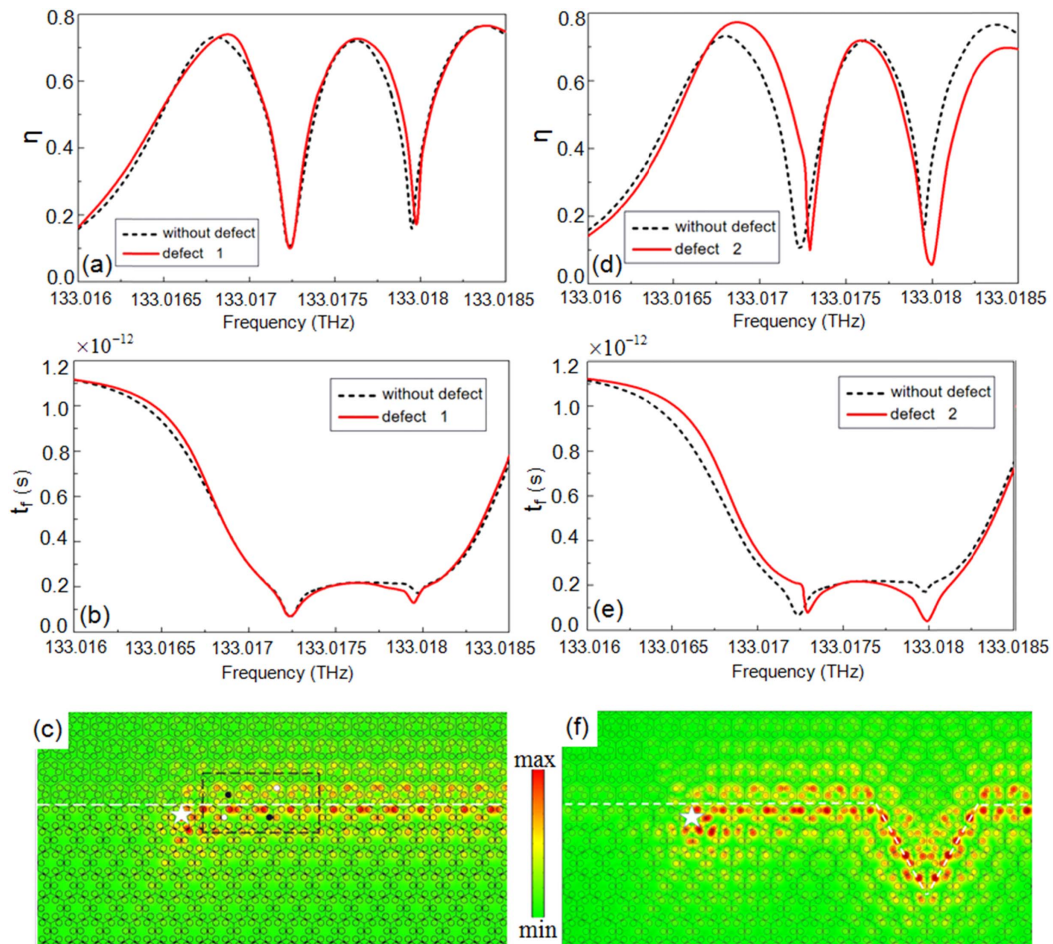
Fig. 4. Topologically protected energy transfer. (a), (b), (c) Case of the first kind of defect; (d), (e), (f) case of the second kind of defect. (a), (d) Energy transfer efficiency (solid red lines) under the two cases; (b), (e) corresponding energy transfer time (solid red lines). The dashed black curves represent the case without defect. (c), (f) Simulated unidirectional propagations of excited interface state along interfaces with disorders (deformed hexagons inside black dashed box) and 60° and 120° turns, respectively. The white star represents the excited chiral light source.

different intrinsic eigenfrequencies of different structures. This means that the present structure can be used to achieve efficient and fast energy transfer over longer distances. This is in contrast to the conventional case, where energy transfer efficiency will decrease sharply with the increase in distance between the donor and the acceptor, and efficient and rapid energy transfer occurs only at a small separation distance.

Another important feature of this platform is that the realized energy transfer is topologically protected, i.e., it is robust against various kinds of defects. In order to exhibit such a phenomenon, we consider two types of defects. One is to introduce intentionally deformed artificial atoms at the interface, and the other is to use a sharply bent interface. Here, $L_2 = 20a$ is taken. The red solid lines in Figs. 4(a) and 4(b) display calculated results for energy transfer efficiency and time with the first kind of defect, and the corresponding results for the second kind of defect are given in Figs. 4(d) and 4(e). For the first defect, as shown in the black dashed rectangle of Fig. 4(c), the black cylinders represent that their positions have moved $0.02a$ to the left, and the white cylinders represent that their radii have reduced to 0.145 μm. For the second defect, the original interface has been replaced by an interface with 60° and 120° turns, as shown in Fig. 4(f). For comparison, the corresponding results without defects are shown by black dashed lines. It can be seen that under the two defects, there is only a slight change in energy transfer efficiency and frequency shift, and the energy transfer time has a slight increase, which exhibits very good robust properties. In order to disclose the origin of these phenomena, the distributions of the electric fields at the interface with defects are plotted in Figs. 4(c) and 4(f) when chiral light sources (marked with stars) are put on the interface. It is found that there is almost no backscattering with disorders. It is the topologically protected channel that leads to the robust energy transfer. Note that we put the source at the position of the interface, not the corner cavity, just because we want to prove that the edge state is topologically protected. In fact, the energy transfer between the two corner cavities is topologically protected, which depends on the robustness of the interface states.

The above results are obtained without considering the effect of scattering loss due to roughness of the cylinders and absorption of the material. In fact, strong scattering loss and absorption do have an influence on the above phenomena [77,78]. However, when the absorption and scattering losses are small, the effect is also small. In the wavelength range we are concerned with above, the absorption of Al_2O_3 cylinders is quite small or even negligible, which has a limited effect on the results of energy transfer. Also, two ends of the designed PhC are metal plates, which make sure that the electromagnetic waves are difficult to scatter into the air. In addition, compared with some traditional methods to realize the interaction between two quantum dots, our method can achieve a longer distance. For example, the long distance of 1.4 μm interaction of two different InAs/GaAs quantum dots in a PhC micro-cavity has been realized [79], which is much shorter than the distance realized (tens to hundreds of micrometers) in our work. More importantly, long-range energy transfer using this scheme is robust against various kinds of defects. Therefore, the design has

more obvious advantages compared with traditional ones, which is very beneficial for practical applications.

4. SUMMARY

Based on the PhC platform with the 1D topologically protected edge state and 0D corner cavities, we have demonstrated that the long-range coherent energy transfer from a donor to an acceptor can be realized. Because the donor and the acceptor have been put into topological cavities, and the energy transfer between them has been fulfilled with the assistance of the topologically protected interface state, such an energy transfer is robust against various disorders and can also occur over very long distances. These results are very important for various applications, such as biological detections, sensors, and quantum information science.

Disclosures. The authors declare no conflicts of interest.

REFERENCES

1. R. van Grondelle, J. P. Dekker, T. Gillbro, and V. Sundstrom, "Energy transfer and trapping in photosynthesis," Biochim. Biophys. Acta (BBA) **1187**, 1–65 (1994).
2. W. Khlbrandt and D. N. Wang, "Three-dimensional structure of plant light-harvesting complex determined by electron crystallography," Nature **350**, 130–134 (1991).
3. V. Vohra, G. Calzaferri, S. Destri, M. Pasini, W. Porzio, and C. Botta, "Toward white light emission through efficient two-step energy transfer in hybrid nanofibers," ACS Nano **4**, 1409–1416 (2010).
4. J. L. He, D. S. Wang, and S. K. Fan, "Opto-microfluidic immunosensors: from colorimetric to plasmonic," Micromachines **7**, 29 (2016).
5. J. Li, S. K. Cushing, F. Meng, T. R. Senty, A. D. Bristow, and N. Wu, "Plasmon-induced resonance energy transfer for solar energy conversion," Nat. Photonics **9**, 601–607 (2015).
6. T. R. Calhoun, N. S. Ginsberg, G. S. Schlaucohen, Y. C. Cheng, M. Ballottari, R. Bassi, and G. R. Fleming, "Quantum coherence enabled determination of the energy landscape in light-harvesting complex II," J. Phys. Chem. B **113**, 16291–16295 (2009).
7. H. Lee, Y. C. Cheng, and G. R. Fleming, "Coherence dynamics in photosynthesis: protein protection of excitonic coherence," Science **316**, 1462–1465 (2007).
8. E. Collini, C. Y. Wong, K. E. Wilk, P. M. Curmi, P. Brumer, and G. D. Scholes, "Coherently wired light-harvesting in photosynthetic marine algae at ambient temperature," Nature **463**, 644–647 (2010).
9. G. D. Scholes, "Quantum-coherent electronic energy transfer: did nature think of it first?" J. Phys. Chem. Lett. **1**, 2–8 (2010).
10. J. Strümpfer, M. Şener, and K. Schulten, "How quantum coherence assists photosynthetic light-harvesting," J. Phys. Chem. Lett. **3**, 536–542 (2012).
11. D. Abramavicius and S. Mukamel, "Energy-transfer and charge-separation pathways in the reaction center of photosystem II revealed by coherent two-dimensional optical spectroscopy," J. Chem. Phys. **133**, 184501 (2010).
12. H. T. Chang and Y. C. Cheng, "Coherent versus incoherent excitation energy transfer in molecular systems," J. Chem. Phys. **137**, 165103 (2012).
13. D. P. S. Mccutcheon and A. Nazir, "Consistent treatment of coherent and incoherent energy transfer dynamics using a variational master equation," J. Chem. Phys. **135**, 114501 (2011).
14. S. Jang, Y. C. Cheng, D. R. Reichman, and J. D. Eaves, "Theory of coherent resonance energy transfer," J. Chem. Phys. **129**, 101104 (2008).

15. E. Harel and G. S. Engel, "Quantum coherence spectroscopy reveals complex dynamics in bacterial light-harvesting complex 2 (LH2)," Proc. Natl. Acad. Sci. USA **109**, 706–711 (2012).

16. R. Hildner, D. Brinks, J. B. Nieder, R. J. Cogdell, and N. F. van Hulst, "Quantum coherent energy transfer over varying pathways in single light-harvesting complexes," Science **340**, 1448–1451 (2013).

17. G. S. Engel, T. R. Calhoun, E. L. Read, T. K. Ahn, T. Mancal, Y. C. Cheng, R. E. Blankenship, and G. R. Fleming, "Evidence for wavelike energy transfer through quantum coherence in photosynthetic systems," Nature **446**, 782–786 (2007).

18. P. Rebentrost, M. Mohseni, and A. Aspuru-Guzik, "Role of quantum coherence and environmental fluctuations in chromophoric energy transport," J. Phys. Chem. B **113**, 9942–9947 (2009).

19. A. Olaya-Castro and C. F. Lee, "Efficiency of energy transfer in a light-harvesting system under quantum coherence," Phys. Rev. B **78**, 085115 (2007).

20. K. Sun, J. Ye, and Y. Zhao, "Path induced coherent energy transfer in light-harvesting complexes in purple bacteria," J. Chem. Phys. **141**, 124103 (2014).

21. M. Mohseni, P. Rebentrost, S. Lloyd, and A. Aspuru-Guzik, "Environment-assisted quantum walks in photosynthetic energy transfer," J. Chem. Phys. **129**, 174106 (2008).

22. Y. Hashimoto, D. Bossini, T. H. Johansen, E. Saitoh, A. Kirilyuk, and T. Rasing, "Frequency and wavenumber selective excitation of spin waves through coherent energy transfer from elastic waves," Phys. Rev. B **97**, 140404(R) (2018).

23. J. Ren, T. Chen, B. Wang, and X. D. Zhang, "Ultrafast coherent energy transfer with high efficiency based on plasmonic nanostructures," J. Chem. Phys. **146**, 144101 (2017).

24. F. D. M. Haldane and S. Raghu, "Possible realization of directional optical waveguides in photonic crystals with broken time-reversal symmetry," Phys. Rev. Lett. **100**, 013904 (2008).

25. L. Lu, J. D. Joannopoulos, and M. Soljacic, "Topological photonics," Nat. Photonics **8**, 821–829 (2014).

26. A. B. Khanikaev and G. Shvets, "Two-dimensional topological photonics," Nat. Photonics **11**, 763–773 (2017).

27. T. Ozawa, H. M. Price, A. Amo, N. Goldman, M. Hafezi, L. Lu, M. C. Rechtsman, D. Schuster, J. Simon, O. Zilberberg, and I. Carusotto, "Topological photonics," Rev. Mod. Phys. **91**, 015006 (2019).

28. Z. Wang, Y. Chong, J. D. Joannopoulos, and M. Soljacic, "Observation of unidirectional backscattering-immune topological electromagnetic states," Nature **461**, 772–775 (2009).

29. Y. Wang, W. Zhang, and X. Zhang, "Tunable topological valley transport in two-dimensional photonic crystals," New J. Phys. **21**, 093020 (2019).

30. K. Fang, Z. Yu, and S. Fan, "Realizing effective magnetic field for photons by controlling the phase of dynamic modulation," Nat. Photonics **6**, 782–787 (2012).

31. M. C. Rechtsman, J. M. Zeuner, Y. Plotnik, Y. Lumer, D. Podolsky, F. Dreisow, S. Nolte, M. Segev, and A. Szameit, "Photonic Floquet topological insulators," Nature **496**, 196–200 (2013).

32. A. B. Khanikaev, S. H. Mousavi, W.-K. Tse, M. Kargarian, A. H. MacDonald, and G. Shvets, "Photonic topological insulators," Nat. Mater. **12**, 233–239 (2013).

33. M. Hafezi, S. Mittal, J. Fan, A. Migdall, and J. M. Taylor, "Imaging topological edge states in silicon photonics," Nat. Photonics **7**, 1001–1005 (2013).

34. M. C. Rechtsman, Y. Plotnik, J. M. Zeuner, D. H. Song, Z. G. Chen, A. Szameit, and M. Segev, "Topological creation and destruction of edge states in photonic graphene," Phys. Rev. Lett. **111**, 103901 (2013).

35. B. Yang, T. Wu, and X. Zhang, "Engineering topological edge states in two dimensional magnetic photonic crystal," Appl. Phys. Lett. **110**, 021109 (2017).

36. L. H. Wu and X. Hu, "Scheme for achieving a topological photonic crystal by using dielectric material," Phys. Rev. Lett. **114**, 223901 (2015).

37. Y. Yang, Y. F. Xu, T. Xu, H.-X. Wang, J.-H. Jiang, X. Hu, and Z. H. Hang, "Visualization of a unidirectional electromagnetic waveguide using topological photonic crystals made of dielectric materials," Phys. Rev. Lett. **120**, 217401 (2018).

38. S. Barik, A. Karasahin, C. Flower, T. Cai, H. Miyake, W. DeGottardi, M. Hafezi, and E. Waks, "A topological quantum optics interface," Science **359**, 666–668 (2018).

39. S. Mittal, E. A. Goldschmidt, and M. Hafezi, "A topological source of quantum light," Nature **561**, 502–506 (2018).

40. M. C. Rechtsman, Y. Lumer, Y. Plotnik, A. Perez-Leija, A. Szameit, and M. Segev, "Topological protection of photonic path entanglement," Optica **3**, 925–930 (2016).

41. A. Blanco-Redondo, B. Bell, D. Oren, B. J. Eggleton, and M. Segev, "Topological protection of biphoton states," Science **362**, 568–571 (2018).

42. S. Mittal, V. V. Orre, and M. Hafezi, "Topologically robust transport of entangled photons in a 2D photonic system," Opt. Express **24**, 15631–15641 (2016).

43. J.-L. Tambasco, G. Corrielli, R. J. Chapman, A. Crespi, O. Zilberberg, R. Osellame, and A. Peruzzo, "Quantum interference of topological states of light," Sci. Adv. **4**, eaat3187 (2018).

44. Y. Wang, Y. H. Lu, F. Mei, J. Gao, Z. M. Li, H. Tang, S. L. Zhu, S. T. Jia, and X. M. Jin, "Direct observation of topology from single-photon dynamics," Phys. Rev. Lett. **122**, 193903 (2019).

45. Y. Wang, X. L. Pang, Y. H. Lu, J. Gao, Y. J. Chang, L. F. Qiao, Z. Q. Jiao, H. Tang, and X. M. Jin, "Topological protection of two-photon quantum correlation on a photonic chip," Optica **6**, 955–960 (2019).

46. G. Harari, M. A. Bandres, Y. Lumer, M. C. Rechtsman, Y. D. Chong, M. Khajavikhan, D. N. Christodoulides, and M. Segev, "Topological insulator laser: theory," Science **359**, eaar4003 (2018).

47. J. Perczel, J. Borregaard, D. E. Chang, S. F. Yelin, and M. D. Lukin, "Topological quantum optics using atomlike emitter arrays coupled to photonic crystals," Phys. Rev. Lett. **124**, 083603 (2020).

48. J. Perczel, J. Borregaard, D. E. Chang, H. Pichler, S. F. Yelin, P. Zoller, and M. D. Lukin, "Topological quantum optics in two-dimensional atomic arrays," Phys. Rev. Lett. **119**, 023603 (2017).

49. W. A. Benalcazar, B. A. Bernevig, and T. L. Hughes, "Quantized electric multipole insulators," Science **357**, 61–66 (2017).

50. C. W. Peterson, W. A. Benalcazar, T. L. Hughes, and G. Bahl, "A quantized microwave quadrupole insulator with topologically protected corner states," Nature **555**, 346–350 (2018).

51. S. G. Marc, P. Valerio, S. Roman, R. B. Osama, L. Tom, G. V. Luis, and D. H. Sebastian, "Observation of a phononic quadrupole topological insulator," Nature **555**, 342–345 (2018).

52. S. Imhof, C. Berger, F. Bayer, J. Brehm, L. W. Molenkamp, T. Kiessling, F. Schindler, C. H. Lee, M. Greiter, T. Neupert, and R. Thomale, "Topolectrical-circuit realization of topological corner modes," Nat. Phys. **14**, 925–929 (2018).

53. J. Noh, W. A. Benalcazar, S. Uang, M. J. Collins, K. P. Chen, T. L. Hughes, and M. C. Rechtsman, "Topological protection of photonic mid-gap defect modes," Nat. Photonics **12**, 408–415 (2018).

54. B. Xie, G. Su, H. Wang, H. Su, X. Shen, P. Zhan, M. Lu, Z. Wang, and Y. Chen, "Visualization of higher-order topological insulating phases in two-dimensional dielectric photonic crystals," Phys. Rev. Lett. **122**, 233903 (2019).

55. Y. Ota, F. Liu, R. Katsumi, K. Watanabe, K. Wakabayashi, Y. Arakawa, and S. Iwamoto, "Photonic crystal nanocavity based on a topological corner state," Optica **6**, 786–789 (2019).

56. X. D. Chen, W. M. Deng, F. L. Shi, F. L. Zhao, M. Chen, and J. W. Dong, "Direct observation of corner states in second-order topological photonic crystal slabs," Phys. Rev. Lett. **122**, 233902 (2019).

57. M. Ezawa, "Higher-order topological insulators and semimetals on the breathing kagome and pyrochlore lattices," Phys. Rev. Lett. **120**, 026801 (2018).

58. X. Ni, M. Weiner, A. Alu, and A. B. Khanikaev, "Observation of higher-order topological acoustic states protected by generalized chiral symmetry," Nat. Mater. **18**, 113–120 (2019).

59. S. Mittal, V. V. Orre, G. Zhu, M. A. Gorlach, A. Poddubny, and M. Hafezi, "Photonic quadrupole topological phases," Nat. Photonics **13**, 692–696 (2019).

60. H. Xue, Y. Yang, F. Gao, Y. Chong, and B. Zhang, "Acoustic higher-order topological insulator on a kagome lattice," Nat. Mater. **18**, 108–112 (2019).

61. X. J. Zhang, H. X. Wang, Z. K. Lin, Y. Tian, B. Y. Xie, M. H. Lu, Y. F. Chen, and J. H. Jiang, "Second-order topology and multidimensional topological transitions in sonic crystals," Nat. Phys. **15**, 582–588 (2019).

62. F. Schindler, Z. J. Wang, M. G. Vergniory, A. M. Cook, A. Murani, S. Sengupta, A. Y. Kasumov, R. Deblock, S. Jeon, I. Drozdov, H. Bouchiat, S. Guéron, A. Yazdani, B. A. Bernevig, and T. Neupert, "Higher-order topology in bismuth," Nat. Phys. **14**, 918–924 (2018).

63. A. El Hassan, F. K. Kunst, A. Moritz, G. Andler, E. J. Bergholtz, and M. Bourennane, "Corner states of light in photonic waveguides," Nat. Photonics **13**, 697–700 (2019).

64. J. Bao, D. Zou, W. Zhang, W. He, H. Sun, and X. D. Zhang, "Topoelectrical circuit octupole insulator with topologically protected corner states," Phys. Rev. B **100**, 201406 (2019).

65. R. Banerjee, S. Mandal, and T. C. H. Liew, "Coupling between exciton-polariton corner modes through edge states," Phys. Rev. Lett. **124**, 063901 (2020).

66. Y. Yang, Z. Jia, Y. Wu, Z.-H. Hang, H. Jiang, and X. C. Xie, "Gapped topological kink states and topological corner states in graphene," Sci. Bull. **65**, 531–537 (2020).

67. X. Xie, W. Zhang, X. He, S. Wu, J. Dang, K. Peng, F. Song, L. Yang, H. Ni, Z. Niu, C. Wang, K. Jin, X. Zhang, and X. Xu, "Topological nanophotonics: cavity quantum electrodynamics with second-order topological corner state (Laser Photonics Rev. 14 (8)/2020)," Laser Photon. Rev. **14**, 1900425 (2020).

68. W. Zhang, X. Xie, H. Hao, J. Dang, S. Xiao, S. Shi, H. Ni, Z. Niu, C. Wang, K. Jin, X. Zhang, and X. Xu, "Low-threshold topological nanolasers based on the second-order corner state," Light Sci. Appl. **9**, 109 (2020).

69. S. Yves, R. Fleury, F. Lemoult, M. Fink, and G. Lerosey, "Topological acoustic polaritons: robust sound manipulation at the subwavelength scale," New J. Phys. **19**, 075003 (2017).

70. Y. Deng, H. Ge, Y. Tian, M. Lu, and Y. Jing, "Observation of zone folding induced acoustic topological insulators and the role of spin-mixing defects," Phys. Rev. B **96**, 184305 (2017).

71. L. Xu, H. Wang, Y. Xu, H. Chen, and J. Jiang, "Accidental degeneracy in photonic bands and topological phase transitions in two-dimensional core-shell dielectric photonic crystals," Opt. Express **24**, 18059–18071 (2016).

72. S. A. H. Gangaraj, G. W. Hanson, and M. Antezza, "Robust entanglement with three-dimensional nonreciprocal photonic topological insulators," Phys. Rev. A **95**, 063807 (2017).

73. H. T. Dung, L. Knöll, and D.-G. Welsch, "Resonant dipoledipole interaction in the presence of dispersing and absorbing surroundings," Phys. Rev. A **66**, 063810 (2002).

74. Z. Ficek and R. Tanas, "Entangled states and collective nonclassical effects in two-atom systems," Phys. Rep. **372**, 369–443 (2002).

75. D. Martín-Cano, A. González-Tudela, L. Martín-Moreno, F. J. García-Vidal, C. Tejedor, and E. Moreno, "Dissipationdriven generation of two-qubit entanglement mediated by plasmonic waveguides," Phys. Rev. B **84**, 235306 (2011).

76. A. Olaya-Castro, C. F. Lee, F. F. Olsen, and N. F. Johnson, "Efficiency of energy transfer in a light-harvesting system under quantum coherence," Phys. Rev. B **78**, 085115 (2008).

77. E. Sauer, J. Pablo Vasco, and S. Hughes, "Theory of intrinsic propagation losses in topological edge states of planar photonic crystals," arXiv:2005.12828 (2020).

78. G. Arregui, J. Gomis-Bresco, C. Marfa Sotomayor-Torres, and P. David García, "Quantifying the robustness of topological slow light," arXiv:2007.15606 (2020).

79. E. Gallardo, L. J. Martínez, A. K. Nowak, D. Sarkar, H. P. van der Meulen, J. M. Calleja, C. Tejedor, I. Prieto, D. Granados, A. G. Taboada, J. M. García, and P. A. Postigo, "Optical coupling of two distant InAs/GaAs quantum dots by a photonic-crystal microcavity," Phys. Rev. B **81**, 193301 (2010).